Article

Soft nanobrush-directed multifunctional MOF nanoarrays

Shuang Wang[1,4], Wenhe Xie[2,4], Ping Wu[3], Geyu Lin[1], Yan Cui[1], Jiawei Tao[1], Gaofeng Zeng [3] ✉, Yonghui Deng [2] ✉ & Huibin Qiu [1] ✉

Controlled growth of well-oriented metal-organic framework nanoarrays on requisite surfaces is of prominent significance for a broad range of applications such as catalysis, sensing, optics and electronics. Herein, we develop a highly flexible soft nanobrush-directed synthesis approach for precise in situ fabrication of MOF nanoarrays on diverse substrates. The soft nanobrushes are constructed via surface-initiated living crystallization-driven self-assembly and their active poly(2-vinylpyridine) corona captures abundant metal cations through coordination interactions. This allows the rapid heterogeneous growth of MOF nanoparticles and the subsequent formation of MIL-100 (Fe), HKUST-1 and CUT-8 (Cu) nanoarrays with tailored heights of 220-1100 nm on silicon wafer, Ni foam and ceramic tube. Auxiliary functional components including metal oxygen clusters and precious metal nanoparticles can be readily incorporated to finely fabricate hybrid structures with synergistic features. Remarkably, the MIL-100 (Fe) nanoarrays doped with Keggin $H_3PMo_{10}V_2O_{40}$ dramatically boost formaldehyde selectivity up to 92.8% in catalytic oxidation of methanol. Moreover, the HKUST-1 nanoarrays decorated with Pt nanoparticles show exceptional sensitivity to H_2S with a ppb-level detection limit.

Nanoarrays that combine the characteristics of nanosize and directional arrangement have aroused widespread attention in a variety of fileds[1–5]. In particular, metal-organic frameworks (MOFs) featuring tailorable pore dimension and chemical functionality present prominent advantages in the construction of multifunctional nanoarrays[6–8]. The uniform alignment of intrinsically porous nanopillars creates a hierarchically open environment for full exposure of active sites and free transfer of reactive substrates, which is favorable for catalysis, sensor, lithium storage, and drug delivery[9–11]. Generally, highly oriented MOF nanoarrays may grow directly on substrates through "one-pot" solvothermal reactions (Fig. 1a). This approach is simple yet powerful, but usually requires selected MOFs with inherent one- or two-dimensional crystalline structures[12,13]. Alternatively, template-directed synthesis is applied to construct multidimensional MOF nanoarrays (Fig. 1b). Notably, metal oxides and hydroxides [e.g., ZnO, CuO, Cu(OH)$_2$ and CoO] arrays have been widely used as hard templates to direct the growth of MOF nanoarrays[14–17]. While these templates facilitate the nucleation of MOFs and rationally direct the growth of MOFs along the templates[18], they normally decompose to release essential metal sources for the growth of desired MOFs. Consequently, the category of MOF nanoarrays is substantially limited by the composition of templates. Besides, it remains a major challenge to handily manipulate the height of the nanoarrays or to simultaneously introduce complementary functional species.

[1]School of Chemistry and Chemical Engineering, Zhangjiang Institute for Advanced Study, Frontiers Science Center for Transformative Molecules, State Key Laboratory of Metal Matrix Composites, Shanghai Jiao Tong University, Shanghai 200240, P. R. China. [2]Department of Chemistry, State Key Laboratory of Molecular Engineering of Polymers, Shanghai Key Laboratory of Molecular Catalysis and Innovative Materials, iChEM, Fudan University, Shanghai 200433, China. [3]CAS Key Laboratory of Low-carbon Conversion Science and Engineering, Shanghai Advanced Research Institute, Chinese Academy of Sciences, 100 Haike Road, Shanghai 201210, China. [4]These authors contributed equally: Shuang Wang, Wenhe Xie. ✉e-mail: zenggf@sari.ac.cn; yhdeng@fudan.edu.cn; hbqiu@sjtu.edu.cn
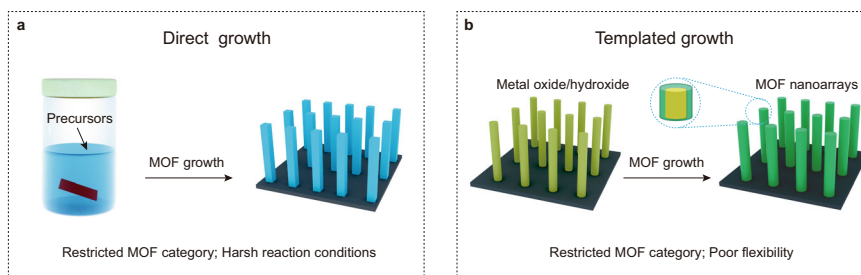
Fig. 1 | Traditional routes to MOF nanoarrays. a Direct growth of MOF nanoarrays under solvothermal conditions. **b** Directed growth of MOF nanoarrays on hard templates.
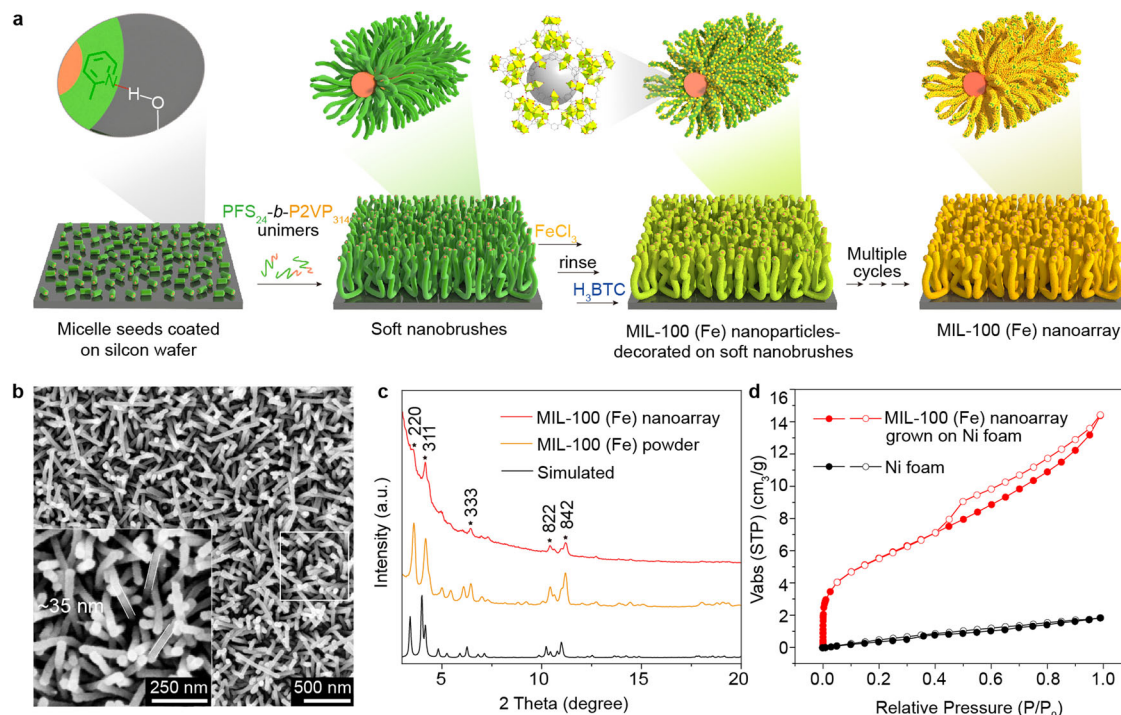
Fig. 2 | Soft nanobrush-directed growth of MIL-100 (Fe) nanoarrays.
a Schematic illustration of the fabrication process. **b** Scanning electron microscope (SEM) images of a nanoarray obtained by alternately immersing a soft nanobrush-coated silicon wafer into ethanol solutions of $FeCl_3$ and H_3BTC for five cycles.

c XRD pattern of the obtained MIL-100 (Fe) nanoarray with comparison to that of the MIL-100 (Fe) powder and simulated XRD pattern of MIL-100 (Fe). **d** N_2 sorption isotherms of a piece of MIL-100 (Fe) nanoarray-decorated Ni foam and a piece of naked Ni foam. Source data are provided as a Source Data file.

Here, we develop a highly flexible soft nanobrush-directed strategy for the precise fabrication of MOF nanoarrays. The soft nanobrushes are facilely introduced onto various substrates via living crystallization-driven self-assembly[19], and their abundant pyridine groups provide the active sites for the capture of copious metal cations to direct the growth of diverse MOFs. By simply immersing in specific precursor solutions, various well-aligned MOF nanoarrays with high aspect ratios and controllable heights can be readily grown on silicon wafer, Ni foam and ceramic tube. Subsequently, polyoxometalates and noble metal nanoparticles are elaborately introduced into the nanoarrays for synergistic catalytic oxidation of methanol and ultrasensitive sensing of hydrogen sulfide.

Results and discussion

Soft nanobrush was firstly prepared on a silicon wafer via surface-initiated living crystallization-driven self-assembly of PFS_{24}-*b*-$P2VP_{314}$ on pre-immobilized PFS_{44}-*b*-$P2VP_{526}$ seeds [PFS = polyferrocenyldimethylsilane, P2VP = poly(2-vinylpyridine), the subscripts refer to the number-average degree of polymerization

of each block] (Supplementary Fig. 1)[19]. The abundant pyridine groups in the P2VP corona were capable to bind with various metal ions through coordination interactions[20]. Initially, $FeCl_3$ and 1,3,5-benzenetricarboxylic acid (H_3BTC) were introduced simultaneously into the soft nanobrush system, but it unfortunately led to the formation of irregular composites (Supplementary Fig. 2). Nevertheless, by alternately immersing the soft nanobrush-coated silicon wafer into ethanol solutions of $FeCl_3$ and H_3BTC at room temperature five times (Fig. 2a), a uniform array of nanorods with a high aspect ratio and an average diameter of ~35 nm was eventually obtained (Fig. 2b). The contour of each nanorod was obviously sharper compared to the soft nanobrush (Supplementary Fig. 3), indicating a fine coating of nanoparticles on the soft nanobrush. Upon further increasing the immersing cycles, the diameter of the nanorods increased to ~43 nm for eight cycles and to ~55 nm for ten cycles (Supplementary Fig. 4). In contrast, no growth of nanoarray was observed on naked silicon wafers (Supplementary Fig. 5). X-ray diffraction (XRD) pattern of the nanoarray revealed relatively strong peaks at 3.5°, 4.1°, 6.4°, 10.4° and 11.2° (Fig. 2c), which can

a   Soft nanobrushes coated on silicon wafers

PFS$_{24}$-*b*-P2VP$_{314}$ unimers
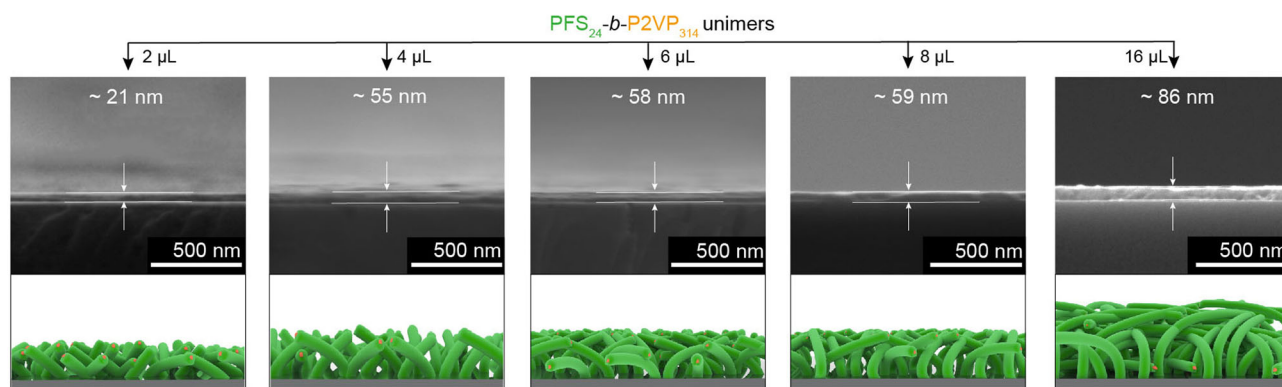
b   MIL-100 (Fe) nanoarrays coated on silicon wafers

MIL-100 (Fe) nanoarray (2 µL)   MIL-100 (Fe) nanoarray (4 µL)   MIL-100 (Fe) nanoarray (6 µL)   MIL-100 (Fe) nanoarray (8 µL)   MIL-100 (Fe) nanoarray (16 µL)
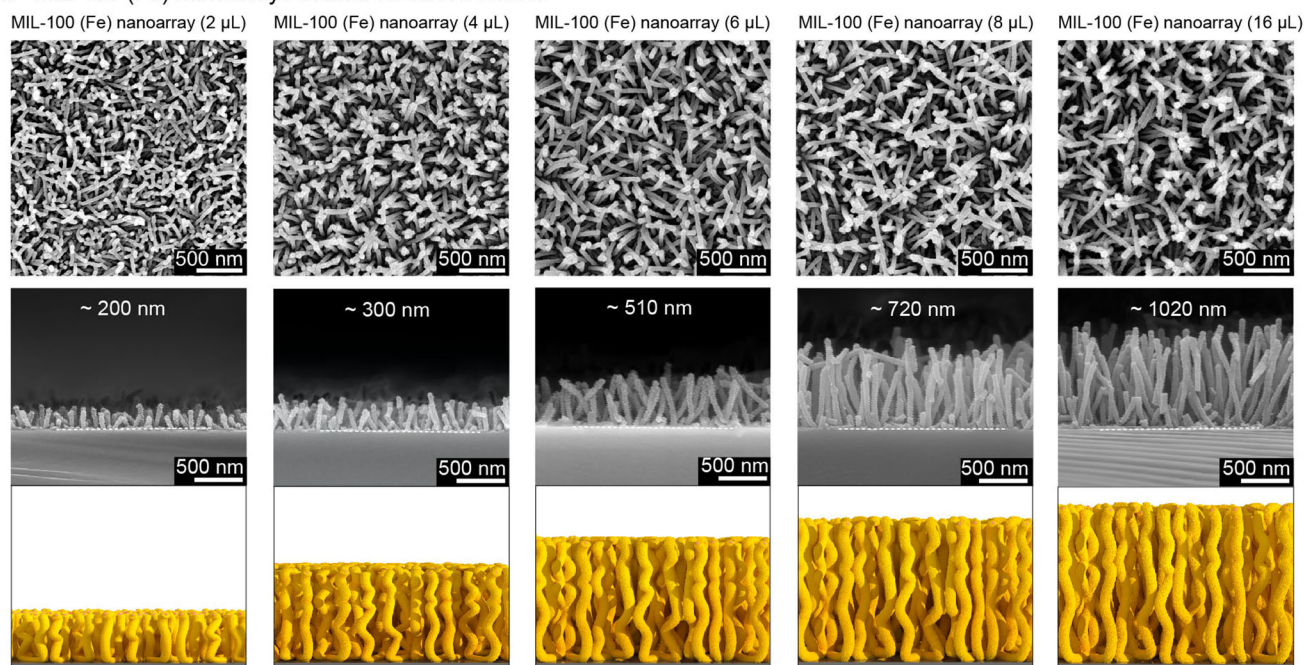
Fig. 3 | Height regulation of MIL-100 (Fe) nanoarrays. a Cross-sectional SEM images of soft nanobrushes formed with the addition of 2, 4, 6, 8 and 16 µL of a THF solution (10 mg/mL) of PFS$_{24}$-*b*-P2VP$_{314}$ unimers. **b** Top-view and cross-sectional SEM images of MIL-100 (Fe) nanoarrays directed by the corresponding soft nanobrushes shown in **a**.

be assigned to the (220), (311), (333), (822) and (842) planes of MIL-100 (Fe), respectively. X-ray photoelectron spectroscopy (XPS) spectra of N 1*s* of the MIL-100 (Fe) nanoarray shifted to a higher binding energy value (399.68 eV) compared to the pristine soft nanobrush (398.96 eV) (Supplementary Fig. 6), indicating a strong coordination interaction between the pyridine groups on the soft nanobrush with the Fe centers in the MIL-100 (Fe) nanoparticles. N$_2$ sorption isotherm of the MIL-100 (Fe) nanoarray grown on a piece of Ni foam (Supplementary Fig. 7) showed a prominent sorption in a low relative pressure region (Fig. 2d), revealing a typical microporous feature for MIL-100 (Fe).

Soft nanobrushes with variable lengths were further used to direct the growth of MIL-100 (Fe) nanoarrays. Cross-sectional SEM images showed that the height of the dried soft nanobrushes gradually increased from ~21 to ~86 nm with the addition 2, 4, 6, 8 and 16 µL of a THF solution of PFS$_{24}$-*b*-P2VP$_{314}$ unimers (Fig. 3a, and Supplementary Fig. 8). In contrast to these mostly collapsed soft nanobrushes, the resultant MIL-100 (Fe) nanoarrays revealed erect morphologies, and

their height was considerably higher and constantly increased from ~220 to ~1100 nm (Fig. 3b and Supplementary Fig. 9). Notably, the MIL-100 (Fe) nanoarrays were comprised of very uniform cylindrical pillars with a constant diameter of ~35 nm from root to top, indicating a highly controllable growth of MIL-100 (Fe) along the soft nanobrush. Generally, the height variation of the MIL-100 (Fe) nanoarrays was almost linearly consistent with the addition of PFS$_{24}$-*b*-P2VP$_{314}$ unimers (i.e. the length of the soft nanobrushes)[19] (Supplementary Fig. 10). Consequently, it is very convenient to modulate the height of the MOF nanoarrays through surface-initiated living crystallization-driven self-assembly.

To explore the synthesis generality, the soft nanobrushes were further employed to direct the growth of HKUST-1 nanoarrays by repeatedly immersing the soft nanobrush-coated silicon wafer into ethanol solutions of Cu(OAC)$_2$ and H$_3$BTC five times (Fig. 4a, see Supplementary Figs. S11–14 for more details). The resultant nanoarrays were also comprised of well-defined rod-like pillars with an average diameter of ~45 nm (Fig. 4b). XRD pattern of the nanoarray revealed
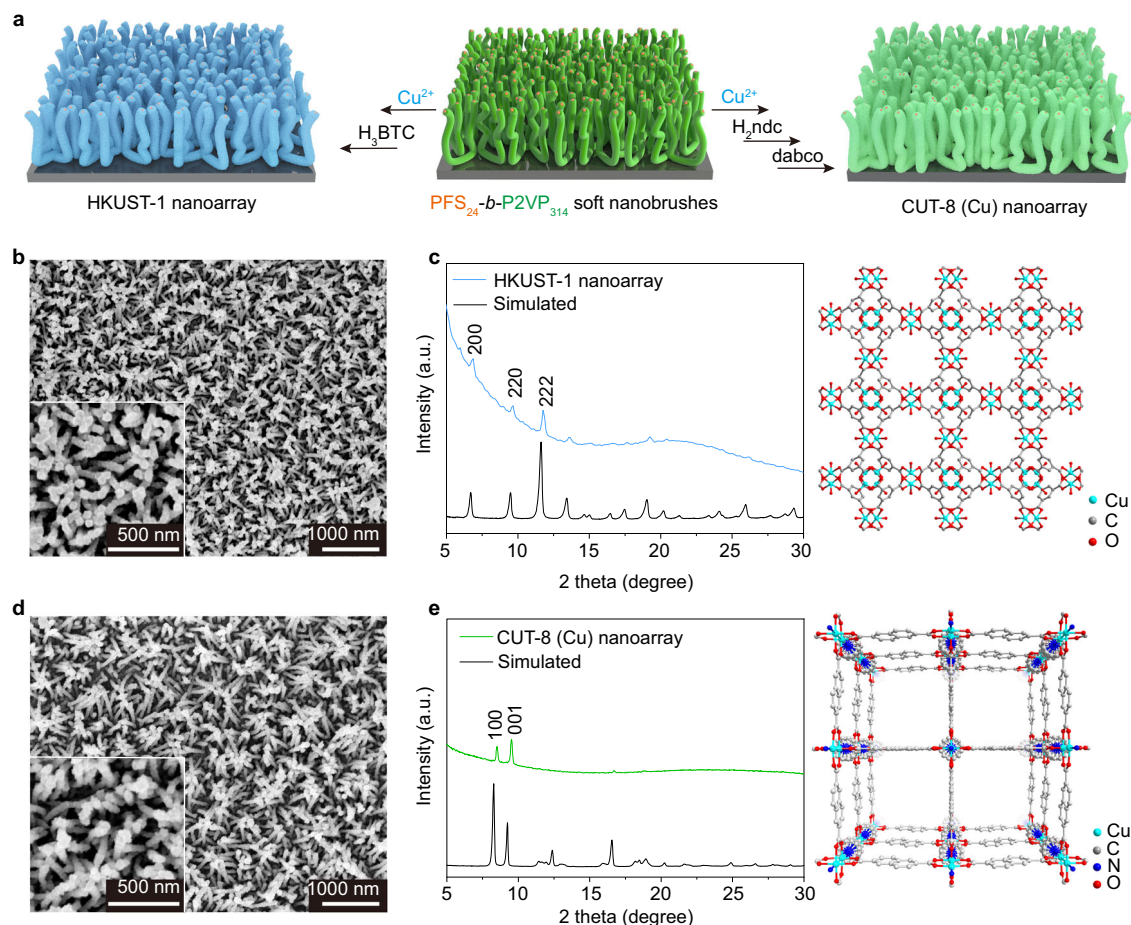
Fig. 4 | Extension of soft nanobrush-directed MOF nanoarrays. a Scheme illustration of the fabrication process for HKUST-1 and CUT-8 (Cu) nanoarrays. **b** SEM images of an HKUST-1 nanoarray obtained by alternately immersing a soft nanobrush-coated silicon wafer into ethanol solutions of Cu(CH₃COO)₂ and H₃BTC for five cycles. **c** XRD pattern of the obtained HKUST-1 nanoarray and simulated XRD pattern of HKUST-1. The right image shows the crystal structure of HKUST-1. **d** SEM images of a CUT-8 (Cu) nanoarray obtained by alternately immersing a soft nanobrush-coated silicon wafer into ethanol solutions of Cu(CH₃COO)₂, H₂ndc and dabco for five cycles. **e** XRD pattern of the obtained CUT-8 (Cu) nanoarray and simulated XRD pattern of CUT-8 (Cu). The right image shows the crystal structure of CUT-8 (Cu). The soft nanobrushes were formed by adding 6 μL of a solution of PFS₂₄-*b*-P2VP₃₁₄ unimers (10 mg/mL in THF). Source data are provided as a Source Data file.

characteristic peaks for HKUST-1 at 6.8° (200), 9.5° (220) and 11.7° (222), respectively (Fig. 4c). High-angle annular dark-field scanning transmission electron microscopy (HAADF-STEM) confirmed the formation of hard rods with a clear profile, and the corresponding element mapping images demonstrated the typical composition of HKUST-1 (Supplementary Fig. 11f). Furthermore, CUT-8 (Cu) nanoarrays with dual-ligands were also fabricated on silicon wafers by repeatedly immersing in ethanol solutions of Cu(OAC)₂, H₂ndc (1,4-naphthalene-bdc) and dabco (1,4-diazabicyclo[2.2.2]octane) (Fig. 4d,e and Supplementary Fig. 15). Hence, the soft nanobrushes are highly promising to direct the growth of diverse MOF nanoarrays, aiming at various functions and applications.

MOF nanoarrays provided a remarkable platform for catalysis in consideration of the open and free space as well as the abundant metallic active sites[9]. It was previously found that Fe-based materials are promising redox catalysts for selective oxidation of CH₃OH into formaldehyde (FA), an important chemical intermediate for polyacetal resin and adhesive, via oxidative dehydrogenation[21–23]. Consequently, the Fe-containing MIL-100 nanoarrays were used to catalyze the oxidation of methanol under industrially relevant conditions (Fig. 5a). Compared to the pristine or supported (immobilized on a silicon wafer) MIL-100 (Fe) powder, the MIL-100 (Fe) nanoarrays (2 μL, 6 μL, 16 μL) showed remarkably higher activity at higher temperatures (>160 °C)

and enabled 100% conversion of methanol over 200 °C (Fig. 5b). As a reflection of the intrinsic activity of the iron center, the turnover frequency (TOF) of the MIL-100 (Fe) nanoarray (16 μL) (216.25 h⁻¹) was also obviously higher than that of the pristine (0.0355 h⁻¹) and supported MIL-100 (Fe) powder (0.773 h⁻¹) (Supplementary Table 1), Besides, the erect MIL-100 (Fe) nanoarray showed a significantly faster reaction rate than the collapsed sample (Supplementary Fig. 16), indicating a faster mass transfer within the highly open MIL-100 (Fe) nanoarray. Besides, the MIL-100 (Fe) nanoarray (16 μL) exhibited a remarkably higher maximum (at 160 °C, Supplementary Fig. 17) FA selectivity of 72.7% compared to the pristine (21.4%) and supported MIL-100 (Fe) powder (20.6%), as well as the soft nanobrush (<20%) (Fig. 5c). It should be noted that the morphology of the MIL-100 (Fe) nanoarrays was well preserved after the catalytic reaction (Supplementary Fig. 18), indicative of superior structural stability.

Previous studies have demonstrated that the addition of vanadium centers can considerably boost the selectivity of FA via promoting the dehydrogenation of CH₃OH molecules[24,25]. However, these vanadium-containing active components were rarely incorporated into MOF arrays probably due to the unfavorable interactions. Fortunately, the P2VP corona of the soft nanobrush can simultaneously bind with the vanadium species in the growth process of MOFs and hence may function as a Trojan horse to incorporate the
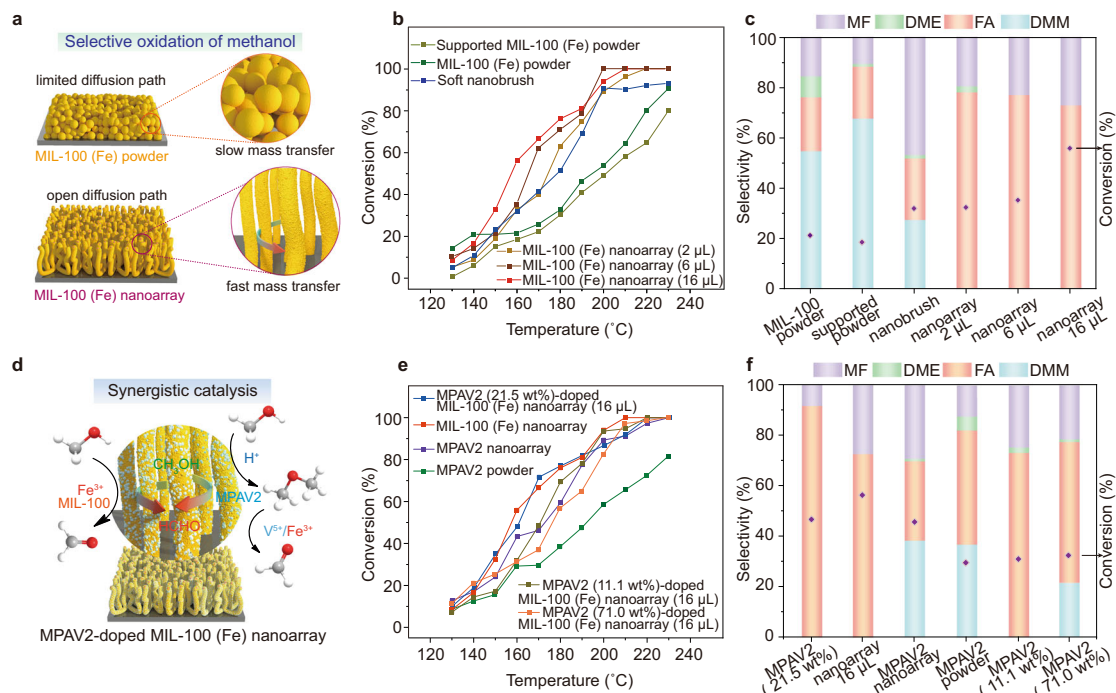
Fig. 5 | Selective oxidation of methanol catalyzed by MIL-100 (Fe) nanoarrays. **a** Schematic illustration of the catalytic environment of a MIL-100 (Fe) nanoarray and a layer of MIL-100 (Fe) powder. **b, c** Temperature dependence of conversion (**b**) and FA selectivity (**c**) at 160 °C for the oxidation of methanol in the presence of the pristine MIL-100 (Fe) powder, MIL-100 (Fe) powder immobilized on a silicon wafer, soft nanobrushes and MIL-100 (Fe) nanoarrays (2 μL, 6 μL, 16 μL), respectively. **d** Schematic illustration of the synergistic catalytic effect between the MIL-100 (Fe) nanoarray and MPAV2 during the oxidation of methanol. **e, f** Temperature dependence of conversion (**e**) and FA selectivity (**f**) at 160 °C for the oxidation of methanol in the presence of the MPAV2 (21.5 wt%)-doped MIL-100 (Fe) nanoarray (16 μL), MIL-100 (Fe) nanoarray (16 μL), MPAV2 nanoarray, MPAV2 powder, MPAV2 (11.1 wt%)-doped MIL-100 (Fe) nanoarray (16 μL) and MPAV2 (71.0 wt%)-doped MIL-100 (Fe) nanoarray (16 μL), respectively. Note: DMM = dimethoxymethane, DME = dimethyl ether. Source data are provided as a Source Data file.

vanadium-based components into the MOF nanoarrays. To this end, the soft nanobrush-coated silicon wafer was additionally immersed in an ethanol solution of vanadium-substituted Keggin polyoxometalate ($H_3PMo_{10}V_2O_{40}$, MPAV2) during the growth of the MIL-100 (Fe) nanoarray (Fig. 5d and Supplementary Fig. 19)[26]. Element mapping of the hybrid nanoarray revealed a uniform distribution of MPVA2 throughout the MIL-100 (Fe) nanorods (Supplementary Fig. 19c). The hybrid nanoarray doped with 21.5 wt% of MPAV2 exhibited an initial reaction rate of 0.0198 mmol·g^{-1}·min^{-1}, which was significantly higher than that of the MIL-100 (Fe) nanoarrays doped with 11.1 and 71.0 wt% of MPAV2, and the collapsed MIL-100 (Fe) doped with 21.5 wt% of MPAV2 (Fig. 5e and Supplementary Fig. 20). Meanwhile, the nanoarray doped with 21.5 wt% of MPAV2 revealed a significantly enhanced FA selectivity of 92.8%, much higher than the MIL-100 (Fe) nanoarray (16 μL) (72.7%), the MPAV2 powder (42.7%), the pristine MPAV2 nanoarray (16 μL) and the previously reported Fe-based materials (Fig. 5f and Supplementary Table 2). These findings demonstrated the presence of a synergistic catalytic effect between the MPVA2 and MIL-100 (Fe), where the abundant Fe^{3+} active sites on the highly aligned MIL-100 (Fe) nanoarray dominate the oxidative dehydrogenation of CH_3OH, while the doped MPAV2 moieties provide additional redox catalytic sites (V^{5+}) and acid sites involved in the acetalization reactions. On the contrary, the phosphotungstic acid PW$_{12}$ only provided the acid sites[27] and hence the PW$_{12}$ (18.6 wt%)-doped MIL-100 (Fe) nanoarray only led to the formation of MF (methyl formate) as the major product (Supplementary Fig. 21). Notably, the morphology and catalytic activity of the nanoarray doped with 21.5 wt% of MPAV2 were well retained after 7 cycles of methanol oxidation (Supplementary Figs. 22, 23), indicative of a high recyclability.

The MOF nanoarrays also provided a promising platform for gas sensing because of the highly open structure and abundant metal

active sites[28]. To this end, the HKUST-1 nanoarrays were specifically grown on the ceramic tubes devices (Fig. 6a and Supplementary Figs. 24, 25) with an aim to study their gas sensing performance toward H$_2$S by taking advantage of the affinity of cupric ions for H$_2$S[29,30]. Unfortunately, the pristine HKUST-1 nanoarrays only showed irreversible response to H$_2$S (1 ppm) even at 200 °C, probably as a consequence of its poor conductivity and strong binding with H$_2$S (Fig. 6d). To solve this problem, Pt nanoparticles were deliberately introduced to the HKUST-1 nanoarray through in situ reduction to improve the conductivity and increase the desorption rate of H$_2$S (Fig. 6b,c and Supplementary Figs. 26–31)[31]. Compared to the pristine HKUST-1 nanoarray (16 μL), the HKUST-1 nanoarray (16 μL) loaded with 0.36 wt% of Pt nanoparticles [HKUST-1 nanoarray (16 μL)/Pt-0.36] displayed a remarkably higher sensitivity and cycling reversibility to 1 ppm H$_2$S at 200 °C and the resistance quickly recovered to the baseline within 17.9 s (Fig. 6e and Supplementary Figs. 32, 33). Meanwhile, the resistance value of the HKUST-1 nanoarray (16 μL)/Pt-0.36 reached 2.1×10^8 Ω, which was a magnitude lower than the pristine HKUST-1 nanoarray (16 μL) (2.3×10^9 Ω). As a parameter to evaluate the desorption dynamics, the recovery time (24.8 s) of the HKUST-1 nanoarray (16 μL)/Pt-0.36 in 1 ppm H$_2$S was apparently shorter than that of the pristine HKUST-1 nanoarrays (over 125 s) and the collapsed HKUST-1 nanoarray (16 μL)/Pt-0.36 (37 s) (Fig. 6f, and Supplementary Figs. 34, 35), indicating a fast desorption of H$_2$S. Besides, the HKUST-1 nanoarray (16 μL)/Pt-0.36 showed a quick response to H$_2$S with various concentrations from 0.1 to 10 ppm (Fig. 6g) and the response value ($S = R_g/R_a$) continuously increased from 1.22 to 7.55 (Fig. 6h). XPS analysis and density functional theory (DFT) calculations both showed that the transformation of H$_2$S molecules is dynamically and thermodynamically more favorable on the HKUST-1/Pt nanoarray (Supplementary Figs. 36–38). Notably, the
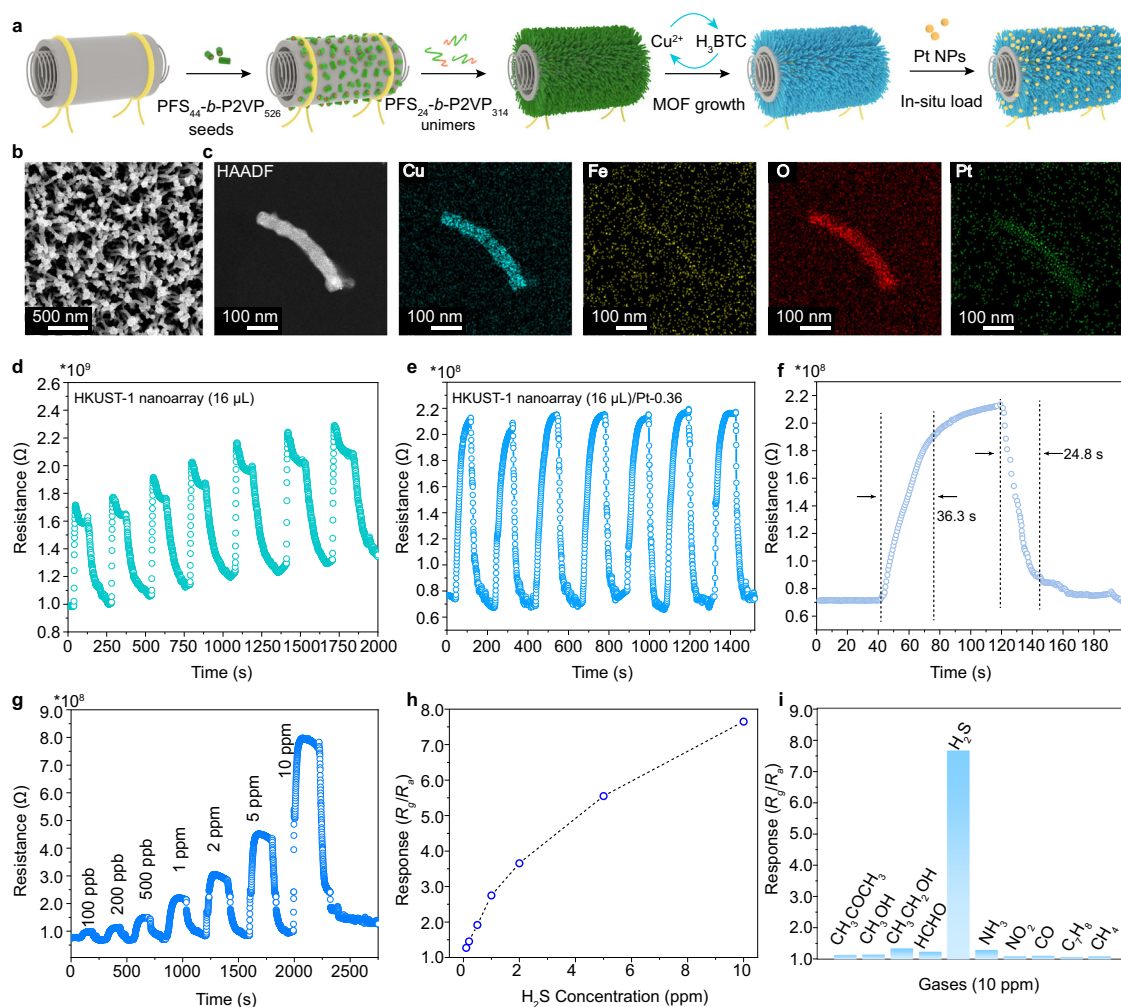
Fig. 6 | Fabrication of HKUST-1 nanoarrays on ceramic tubes and their gas sensing performance. a Schematic illustration of the fabrication process of HKUST-1 nanoarray on a ceramic tube and the further loading of Pt nanoparticles. **b** SEM image of the HKUST-1 nanoarray (16 μL)/Pt-0.36. **c** HRTEM image and element mapping of the HKUST-1 nanoarray (16 μL)/Pt-0.36. **d** Repeating response-recovery curve of the pristine HKUST-1 nanoarray (16 μL) to 1 ppm of H_2S at 200 °C. **e** Repeating response-recovery curve of the HKUST-1 nanoarray (16 μL)/Pt-0.36 to 1 ppm of H_2S at 200 °C. **f** Fine analysis of a response-recovery cycle of the HKUST-1 nanoarray (16 μL)/Pt-0.36 to 1 ppm H_2S at 200 °C. **g** Response-recovery curve of the HKUST-1 nanoarray (16 μL)/Pt-0.36 to H_2S of different concentrations at 200 °C. **h** Response ($S = R_g/R_a$) of the HKUST-1 nanoarray (16 μL)/Pt-0.36 versus H_2S concentration. **i** Responses of the HKUST-1 nanoarray (16 μL)/Pt-0.36 to different chemical vapors (10 ppm) at 200 °C. Source data are provided as a Source Data file.

HKUST-1 nanoarray (16 μL)/Pt-0.36 achieved an ultrahigh selectivity toward H_2S at 10 ppm with negligible response to the other interference chemical vapors (Fig. 6i). Moreover, the sensing performance of the HKUST-1 nanoarray (16 μL)/Pt-0.36 remained at a relatively high level over 2 weeks (Supplementary Fig. 39). Compared to the conventional sensing materials, the HKUST-1 nanoarray (16 μL)/Pt-0.36 displayed a prominent comprehensive sensing performance (Supplementary Table 3).

In summary, a soft nanobrush-directed growth strategy was developed for precise fabrication of MIL-100 (Fe), HKUST-1 and CUT-8 (Cu) nanoarrays on diverse substrates. The height of MOF nanoarrays was readily tailored from ~220 nm to ~1100 nm by precisely controlling the length of soft nanobrushes. The soft nanobrushes also provided an extremely flexible platform for efficient incorporation of a variety of complementary functional species, aiming at diverse synergistic features. Notably, additional doping of Keggin-type MPAV2 into the MIL-100 (Fe) nanoarray further improved the selectivity of FA to a remarkable value of 92.8% for the oxidation of methanol. Besides, the HKUST-1 nanoarrays loaded with 0.36 wt% of Pt nanoparticles presented exceptional sensitivity to H_2S along with prominent cycling stability. It is expected that the soft nanobrush template approach

demonstrated in this work would not only facilitate the growth of more types of MOFs but also offer a facile pathway to other inorganic functional nanoarrays.

Methods

Preparation of MIL-100 (Fe) nanoarray on silicon wafer

Typically, a silicon wafer coated with the PFS-*b*-P2VP soft nanobrush was immersed alternately in an ethanolic solution of $FeCl_3·6H_2O$ (10 mM, 1 mL) for 10 min and then in an ethanolic solution of 1,3,5-benzene tricarboxylic acid (H_3BTC) (10 mM, 1 mL) for 10 min at room temperature in a static reaction vessel. Between each step, the sample was rinsed with 1 mL of ethanol to remove the excess reagent. This process was repeated 5 times and the resulting sample was then lyophilized to obtain the MIL-100 (Fe) nanoarray.

Preparation of MIL-100 (Fe) nanoarray on Ni foam

Typically, a piece of Ni foam coated with the PFS-*b*-P2VP soft nanobrush was immersed alternately in an ethanolic solution of $FeCl_3·6H_2O$ (10 mM, 1 mL) for 10 min and then in an ethanolic solution of 1,3,5-benzene tricarboxylic acid (H_3BTC) (10 mM, 1 mL) for 10 min at room temperature in a static reaction vessel. Between each step, the sample

was rinsed with 1 mL of ethanol to remove the excess reagent. This process was repeated 5 times and the resulting sample was then lyophilized to obtain the MIL-100 (Fe) nanoarray.

Preparation of HKUST-1 nanoarray on silicon wafer

Typically, a silicon wafer coated with the PFS-*b*-P2VP soft nanobrush was dipped alternately in an ethanolic solution of $(Cu(CH_3COO)_2 \cdot H_2O$ (10 mM, 1 mL)) for 10 min and then in an ethanolic solution of 1,3,5-benzene tricarboxylic acid (H_3BTC) (10 mM, 1 mL) for 10 min at room temperature in a static reaction vessel. Between each step, the sample was rinsed with 1 mL of ethanol to remove the excess reagent. This process was repeated 5 times and the resulting sample was then lyophilized to obtain the HKUST-1 nanoarray. The HKUST-1 nanoarray was grown on a ceramic tube via a similar procedure.

Preparation of CUT-8 (Cu) nanoarray on silicon wafer

Typically, a silicon wafer coated with the PFS-*b*-P2VP soft nanobrush was dipped alternately in an ethanolic solution of $(Cu(CH_3COO)_2 \cdot H_2O$ (2 mM, 1 mL)) for 10 min, an ethanolic solution of H_2ndc (0.2 mM, 1 mL) for 10 min and an ethanolic solution of dabco (0.2 mM, 1 mL) for 10 min at room temperature in a static reaction vessel. Between each step, the sample was rinsed with 1 mL of ethanol to remove excess reagent. This process was repeated 5 times and the resulting sample was then lyophilized to obtain the CUT-8 (Cu) nanoarray.

Preparation of MPAV2-doped MIL-100 nanoarray on silicon wafer

Typically, a silicon wafer coated with the PFS-*b*-P2VP soft nanobrush was dipped alternately in a mixed solution of water and ethanol (1:1 (v:v)) of MPAV2 (1 mM, 1 mL), an ethanolic solution of $FeCl_3 \cdot 6H_2O$ (10 mM, 1 mL) for 10 min and an ethanolic solution of 1,3,5-benzene tricarboxylic acid (H_3BTC) (10 mM, 1 mL) for 10 min at room temperature in a static reaction vessel. Between each step, the sample was rinsed with 1 mL of ethanol to remove the excess reagent. This process was repeated 5 times and the resulting sample was then lyophilized to obtain the MPAV2-doped MIL-100 (Fe) nanoarray. PW_{12}-doped MIL-100 (Fe) nanoarray was also fabricated via a similar procedure.

Preparation of Pt-loaded HKUST-1 nanoarrays on ceramic tube

In a typical process, the ceramic tube coated with the HKUST-1 nanoarray was firstly placed in 0.5 mL of isopropanol and then 1 μL of an aqueous solution of $Na_2PtCl_4 \cdot 6H_2O$ (1 mM) was added, and the mixture was shacked for 2 h. Subsequently, a chilled aqueous solution of $NaBH_4$ (37.5 μL) was quickly added and the mixture was shaken on an oscillator for 20 min to allow the in situ formation of Pt nanoparticles. The resulting sample was rinsed with isopropanol and further lyophilized to obtain the Pt-loaded HKUST-1 nanoarray.

Catalytic oxidation of methanol

The oxidation of methanol was performed in a fixed-bed tubular reactor with an inner diameter of 12 mm and a length of 550 mm. The catalyst sample was mixed with quartz sand (1.0 g) and then loaded into the reactor. Methanol was introduced into the reactor with a liquid hourly space velocity (LHSV) of 0.19 h^{-1} by a constant flow pump along with a flow of O_2 (22.5 mL/min) and the gas hourly space velocity (GHSV) of reactant gases (methanol and oxygen) was 2832 mL/h/g. The products were analyzed by an on-line GC equipped with a thermal conductivity detector (TCD) and a Porapake-T column. The reaction was performed at atmospheric pressure and the gas lines between the reactor and GC were kept at 120 °C. The product selectivity was calculated as S_i (%) = $n_i/\sum n_i \times 100$%, where i represents the specific product $(CH_3OCH_2OCH_3, HCOOCH_3, HCHO, CH_3OCH_3, CO, or CO_2)$, and n_i is the carbon atom molar of the specific product i.

Gas sensing

The gas sensing tests were operated on a MA1.0 gas sensing measuring system (Narui Corp.Ltd., China). An alumina tube with a pair of printed Au electrodes printed on the black was used to support the sensing materials. A Ni-Cr alloy wire was equipped as a heater to provide tunable working temperature for sensing materials by applying a certain voltage. The assembled sensing device was then seated onto a PCB support with a pair of electrodes attached to the materials and allowed to age at 150 °C for 2 days to remove the excess solvent molecules in the MOF nanoarray. Target analyte, such as hydrogen sulfide, was passed into the gas sensor. The gas response of the sensor in this study was defined as $S = R_g/R_a$, where R_a is the sensor resistance in air and R_g is that in the gas tested. The response time was defined as the time required for the variation in conductance to reach 90% of the equilibrium value after a test gas was injected, and the recovery time was the time required for the sensor to return to 10% above the original conductance in air after releasing the test gas, respectively.

Data availability

Source data are provided with this paper.

References

1. Ong, W. L. et al. Surface chemistry mediates thermal transport in three-dimensional nanocrystal arrays. *Nat. Mater.* **12**, 410–415 (2013).
2. Yang, Y. et al. Directing reconfigurable DNA nanoarrays. *Science.* **357**, 352–353 (2017).
3. Li, H. et al. Systematic design of superoleophobic nanotube-array electrode comprised of transition-metal sulfides for overall water splitting. *Nat. Commun.* **9**, 2452 (2018).
4. Jenkins, J. et al. Antibacterial effects of nanopillar surfaces are mediated by cell impedance, penetration and induction of oxidative stress. *Nat. Commun.* **11**, 1626 (2020).
5. Ji, L. et al. Highly selective electrochemical reduction of CO_2 to alcohols on a FeP nanoarray. *Angew. Chem. Int. Ed.* **59**, 758–762 (2020).
6. Furukawa, H. et al. The chemistry and applications of metal-organic frameworks. *Science.* **341**, 974–986 (2013).
7. Zhang, Z. et al. Template-directed synthesis of metal-organic materials. *Chem. Soc. Rev.* **43**, 5444–5455 (2014).
8. Meng, J. et al. Advances in metal-organic framework coatings: versatile synthesis and broad applications. *Chem. Soc. Rev.* **49**, 3142–3186 (2020).
9. Cheng, W. et al. Lattice-strained metal-organic-framework arrays for bifunctional oxygen electrocatalysis. *Nat. Energy* **4**, 115–122 (2019).
10. Zhou, D., Ni, J. & Li, L. Self-supported multicomponent CPO-27 MOF nanoarrays as high-performance anode for lithium storage. *Nano Energy* **57**, 711–717 (2019).
11. Lin, Y. et al. Layer-by-layer growth of preferred-oriented MOF thin film on nanowire array for high-performance chemiresistive sensing. *Angew. Chem. Int. Ed.* **60**, 25758–25761 (2021).
12. Duan, J. et al. Ultrathin metal-organic framework array for efficient electrocatalytic water splitting. *Nat. Commun.* **8**, 15341 (2017).
13. Hou, R. et al. Integrated conductive hybrid architecture of metal-organic framework nanowire array on polypyrrole membrane for all-solid-state flexible supercapacitors. *Adv. Energy Mater.* **10**, 1901892 (2020).
14. Ma, T. Y. et al. Metal-organic framework derived hybrid Co_3O_4-carbon porous nanowire arrays as reversible oxygen evolution electrodes. *J. Am. Chem. Soc.* **136**, 13925–13931 (2014).
15. Falcaro, P. et al. Centimetre-scale micropore alignment in oriented polycrystalline metal-organic framework films via heteroepitaxial growth. *Nat. Mater.* **16**, 342–348 (2017).

16. Cai, G. et al. Template-directed growth of well-aligned MOF arrays and derived self-supporting electrodes for water splitting. *Chem.* **2**, 791–802 (2017).

17. Zhou, K. et al. Template-directed growth of hierarchical MOF hybrid arrays for tactile sensor. *Adv. Funct. Mater.* **30**, 2001296 (2020).

18. Zhang, W. et al. Nanowire-directed templating synthesis of metal-organic framework nanofibers and their derived porous doped carbon nanofibers for enhanced electrocatalysis. *J. Am. Chem. Soc.* **136**, 14385–14388 (2014).

19. Cai, J. D. et al. Tailored multifunctional micellar brushes via crystallization-driven growth from a surface. *Science* **366**, 1095–1098 (2019).

20. Lin, G. Y. et al. Capillary-bound dense micelle brush supports for continuous flow catalysis. *Angew. Chem. Int. Ed.* **60**, 24637–24643 (2021).

21. Bauer, I. et al. Iron catalysis in organic synthesis. *Chem Rev.* **115**, 3170–3387 (2015).

22. Raun, K. V. et al. Deactivation behavior of an iron-molybdate catalyst during selective oxidation of methanol to formaldehyde. *Catal. Sci. Technol.* **8**, 4626–4637 (2018).

23. Candelaria, S. L. et al. Multi-component Fe-Ni hydroxide nanocatalyst for oxygen evolution and methanol oxidation reactions under alkaline conditions. *ACS Catalysis.* **7**, 365–379 (2016).

24. Routray, K. et al. Catalysis science of methanol oxidation over iron vanadate catalysts: nature of the catalytic active sites. *ACS Catalysis.* **1**, 54–66 (2010).

25. Molinari, J. E. et al. Dynamic surface structures and reactivity of vanadium-containing molybdophosphoric acid ($H_{3+x}PMo_{12-x}V_xO_{40}$) Keggin catalysts during methanol oxidation and dehydration. *ACS Catalysis.* **1**, 1536–1548 (2011).

26. Bruckman, K. et al. Catalytic behavior of unsupported and heteropolysalt-supported $H_{3+n}PMo_{12-n}V_nO_{40}$ heteropolyacides in the test reaction of CH_3OH oxidation. *J. Catal.* **139**, 455–467 (1993).

27. Nandiwale, K. Y. et al. One-pot cascade conversion of renewable furfural to levulinic acid over a bifunctional $H_3PW_{12}O_{40}/SiO_2$ catalyst in the absence of external H_2. *Energy & Fuels.* **35**, 539–545 (2020).

28. Kreno, L. E. et al. Metal-organic framework materials as chemical sensors. *Chem Rev.* **112**, 1105–1125 (2012).

29. Ma, Y. et al. H_2S-activable MOF nanoparticle photosensitizer for effective photodynamic therapy against cancer with controllable singlet-oxygen release. *Angew. Chem. Int. Ed.* **56**, 13752–13756 (2017).

30. Martínez-Ahumada, E. et al. MOF materials for the capture of highly toxic H_2S and SO_2. *Organometallics.* **39**, 883–915 (2020).

31. Ma, J. et al. Pt nanoparticles sensitized ordered mesoporous WO_3 semiconductor: gas sensing performance and mechanism study. *Adv. Func. Mater.* **28**, 1705268 (2017).

Acknowledgements

Author contributions

S.W. and H.Q. conceived the project. S.W. prepared the soft nano-brushes with assistance from G.L.; S.W. prepared the MOF nanoarrays; S.W., P.W. and G.Z. performed the catalytic experiments; Y.C. and J.T. performed the HR-TEM; S.W., W.X. and Y.D. performed the gas sensing experiments; S.W. and H.Q. analyzed the data and prepared the manuscript with input from all the other authors. The project was supervised by H.Q.

Competing interests

The authors declare no competing interests.

Additional information

Supplementary information The online version contains supplementary material available at https://doi.org/10.1038/s41467-022-34512-1.

Correspondence and requests for materials should be addressed to Gaofeng Zeng, Yonghui Deng or Huibin Qiu.

Peer review information *Nature Communications* thanks the anonymous reviewer(s) for their contribution to the peer review of this work.

Reprints and permissions information is available at http://www.nature.com/reprints

Publisher's note Springer Nature remains neutral with regard to jurisdictional claims in published maps and institutional affiliations.